Pressure-driven fragmentation of multiphase clouds at high redshift

H. Dhanoa,[1]⋆ J. Mackey[2] and J. Yates[1]

[1]*Department of Physics and Astronomy, University College London, Gower Street, London WC1E 6BT, UK*
[2]*Argelander-Institut für Astronomie, Auf dem Hügel 71, Bonn D-53121, Germany*

ABSTRACT

The discovery of a hyper metal-poor star with total metallicity of $\leq 10^{-5} \, Z_\odot$ has motivated new investigations of how such objects can form from primordial gas polluted by a single supernova. In this paper, we present a shock-cloud model which simulates a supernova remnant interacting with a cloud in a metal-free environment at redshift $z = 10$. Pre-supernova conditions are considered, which include a multiphase neutral medium and H II region. A small dense clump ($n = 100$ cm^{-3}), located 40 pc from a 40 M$_\odot$ metal-free star, embedded in an $n = 10$ cm^{-3} ambient cloud. The evolution of the supernova remnant and its subsequent interaction with the dense clump is examined. We include a comprehensive treatment of the non-equilibrium hydrogen and helium chemistry and associated radiative cooling that is occurring at all stages of the shock-cloud model, covering the temperature range $10-10^9$ K. Deuterium chemistry and its associated cooling are not included because the UV radiation field produced by the relic H II region and supernova remnant is expected to suppress deuterium chemistry and cooling. We find a 10^3 times density enhancement of the clump (maximum density $\approx 78\,000$ cm^{-3}) within this metal-free model. This is consistent with Galactic shock-cloud models considering solar metallicity gas with equilibrium cooling functions. Despite this strong compression, the cloud does not become gravitationally unstable. We find that the small cloud modelled here is destroyed for shock velocities $\gtrsim 50$ km s^{-1}, and not significantly affected by shocks with velocity $\lesssim 30$ km s^{-1}. Rather specific conditions are required to make such a cloud collapse, and substantial further compression would be required to reduce the local Jeans mass to sub-solar values.

Key words: stars: formation – supernovae: general – galaxies: high-redshift.

1 INTRODUCTION

The first galaxies are thought to have formed around redshift $z \geq 10$ when the universe was less than 500 Myr old. These nascent environments are considered to be the key sites where the transition from Population III to Population II stars took place. A possible fossil from this era is SDSS J102915+172927, which is a low-mass ($M < 0.8$ M$_\odot$) star with a total metallicity of $Z < 10^{-5}$ Z$_\odot$ (Caffau et al. 2011). As a result of such low metallicity, it is deduced that the star formed from primordial gas which was polluted by a single supernova (SN). This star has challenged the theory that a critical metallicity is needed to form sub-solar-mass Population II star (Klessen, Glover & Clark 2012). A better understanding of star formation and its feedback effects at high redshifts is extremely important in relation to the formation of such objects.

While it is important to study star formation at very low metallicity (Nagakura, Hosokawa & Omukai 2009; Chiaki, Yoshida & Kitayama 2013), one cannot evaluate the effects of tiny metal abundances without also studying primordial gas. The metal-free problem is the limiting case, and is therefore very useful as a baseline study for comparison to later calculations for gas that is polluted by trace amounts of metals. It is also very interesting in its own right, because we still do not know if stars of mass <1 M$_\odot$ can form at zero metallicity (see e.g. the interesting proposal presented by Stacy & Bromm 2014).

Here, we examine the shock-cloud interaction model developed by Mackey, Bromm & Hernquist (2003), in which shock compression and subsequent cooling can decrease the Jeans mass in primordial gas, thereby forming lower mass stars than would form without the shock collision. Our work is the first to investigate this problem with detailed multidimensional simulations for metal-free gas. Radiative cooling is the critical factor in promoting hydrodynamic and gravitational instabilities. Therefore, in this paper, we focus on the non-equilibrium cooling that dominates this system. This can only be captured correctly by including non-equilibrium chemistry (linked to thermal models) for the full temperature range associated with an SN shock model. We have focused on hydrogen and helium chemistry because we expect that the environment surrounding a progenitor Population III star is dominated by H$_2$

⋆ E-mail: hd@star.ucl.ac.uk

cooling. Both the relic H II region and the SN remnant are sources of diffuse UV radiation that suppresses HD cooling, so we have not included deuterium chemistry in this work. Wolcott-Green, Haiman & Bryan (2011) showed that HD cooling is strongly suppressed by UV radiation fields that are up to five orders of magnitude weaker than what is required to suppress H_2 cooling.

Kitayama & Yoshida (2005) and Vasiliev, Vorobyov & Shchekinov (2008) highlighted the important link between the radial distribution of primordial gas prior to the SN explosion and the subsequent evolution of the SN remnant, and therefore the formation of extremely metal-poor stars. Consequently, we include both the H II region and neutral medium, to obtain a realistic SN shell evolution. Once the SN shock begins to travel within neutral matter, it interacts with a multiphase medium (Reach, Rho & Jarrett 2005), which cannot be characterized by a single density. Greif et al. (2008) have found that turbulence driven by cold accretion on to a protogalaxy produces a primordial interstellar medium (ISM) with a large range of densities and temperatures. The pressure-driven compression and fragmentation of dense clumps found in this neutral matter could be a possible site for low-mass star formation.

At present, most SN shock models for the early universe only include non-equilibrium cooling for temperatures below 10^4 K and focus on the fragmentation of the SN shell itself. Machida et al. (2005) were the first to investigate primordial low-mass star formation at high redshift via this method. The authors included non-equilibrium cooling from H_2 and HD molecules, coupled to a semi-analytic dynamic model. They found that shell fragmentation was possible for explosion energies $\geq 10^{51}$ erg and ambient density $n > 3$ cm^{-3}. The contraction of the fragments was studied, and the Jeans mass was reduced to $\sim 1\,M_\odot$. Nagakura et al. (2009) extended this model to include metal-line cooling for low-metallicity gas coupled to a 1D hydrodynamic code. They use linear perturbation analysis of the expanding shell to constrain the criteria for fragmentation and found that there is little dependence on metallicity in the range 10^{-4}–$10^{-2}\,Z_\odot$. Compared to Machida et al. (2005), they found that fragmentation only occurred in higher ambient uniform densities ($n \geq 100$ cm^{-3} for a 10^{51} erg explosion and $n \geq 10$ cm^{-3} for a 10^{52} erg explosion), and eventually form fragments of mass 10^2–$10^3\,M_\odot$.

Chiaki et al. (2013) developed a 1D SN model that considers a gas with metallicity $10^{-5}\,Z_\odot$. The authors include metal-free non-equilibrium chemistry for temperatures below 10^4 K, with separate calculated rates for metal-line cooling. However, above 10^4 K, the authors utilize the collisional ionization equilibrium cooling function by Sutherland & Dopita (1993). The authors find that the SN shell becomes gravitationally unstable for a wide range of explosion energies (10^{51}–3×10^{52} erg) and ambient uniform densities ($n \geq 10$ cm^{-3}). The thermal evolution of a shell fragment was followed using a one-zone model (a point calculation) which includes low-metallicity chemistry and dust cooling. They expect the fragment to evolve into a high-density core (10^{13} cm^{-3}), which will eventually form multiple clumps of mass 0.01–0.1 $M_\odot$.

Using a one-zone model, Mackey et al. (2003) modelled an equilibrium primordial gas cloud that is shocked by an SN. The shocked cloud is heated to a higher entropy state and it is assumed to cool isobarically back to its original equilibrium temperature, but now at a much higher density than before. In this way, the Jeans mass of the gas could be reduced by a large factor, allowing much lower mass stars to form. This argument also applies to smooth ISM distributions, as discussed above (Machida et al. 2005; Nagakura et al. 2009; Chiaki et al. 2013), as long as isobaric conditions hold in the decelerating shell.

The one-zone model of Mackey et al. (2003) also crucially depends on the isobaric assumption to increase the gas density in the cooling cloud. In reality, however, pressure is a decreasing function of time in an SN remnant, because the explosion is (by definition) vastly overpressurised compared to its surroundings. As long as the expansion time-scale of the SN $t_{\mathrm{exp}} = R_{\mathrm{sh}}/\dot{R}_{\mathrm{sh}}$ (where R_{sh} is the shock radius and $\dot{R}_{\mathrm{sh}}$ its velocity) is short compared to the local time-scale for gravitational effects (i.e. the free-fall time $t_{\mathrm{ff}} = 1/\sqrt{G\rho}$, where ρ is the gas density and G the gravitational constant), then the time-dependence of the external pressure is an important part of the solution. The passage of a strong shock through a dense cloud can also have catastrophic consequences for the cloud (Klein, McKee & Colella 1994) through turbulent hydrodynamic instabilities. Both of these considerations are best addressed with multidimensional hydrodynamic simulations and cannot be captured in one-zone models.

Melioli et al. (2006) investigated star formation triggered in the Galactic environment, via the interaction of an SN shell and molecular cloud. The authors produce constraints on cloud collapse (and therefore possible star formation) in the 'SN remnant radius versus cloud density' parameter space. This was achieved by an analytic study comparing the gravitational free-fall time and destruction time-scale of the cloud (which depends on a number of parameters including radiative cooling). By running a suite of 3D hydrodynamic simulations, they were able to confirm that these numerical models were consistent with their analytic constraints. The authors recognize that using an approximate polytropic pressure equation to represent radiative cooling may be an oversimplification and more realistic cooling functions are required.

Johansson & Ziegler (2013) have concentrated on the compression of smaller clouds (radius ~ 1 pc) found in the local ISM as a method of triggered star formation. Their magnetohydrodynamic simulations (without self-gravity) concentrate on the radiative interaction between the shock and the cloud. The cooling function utilized is a piecewise power law given by Sánchez-Salcedo, Vázquez-Semadeni & Gazol (2002) and Slyz et al. (2005), and assumes collisional ionization equilibrium. They find that the cloud fragments into small dense cool clumps and do not become Jeans unstable. Importantly, they find that initial density enhancements within the cloud can increase by a factor of 10^3–10^5, which eventually relaxes to a final density enhancement of 10^2–10^3. This is consistent with results by Vaidya, Hartquist & Falle (2013), who have a similar model which includes self-gravity. They find that gravity does not contribute to the large increase in density but plays an important role by preventing the re-expansion of the high-density region.

These studies have highlighted that radiative cooling is a crucial process in the interaction between shocks and clouds. In this paper, we simulate an SN exploding in a metal-free environment and include the non-equilibrium radiative cooling that occurs at all stages of its evolution and subsequent collision with a multiphase neutral cloud. The diffusion of the metals is neglected and the system is approximated by primordial chemistry. Hence, we present a model which includes the non-equilibrium metal-free chemistry and its associated cooling for the evolution of a supernova shell and its subsequent interaction of a small dense clump embedded in a neutral cloud at redshift $z = 10$. In Section 2, we outline how the initial conditions are generated by the pre-SN model, and introduce the chemo-dynamic modelling of the SN remnant. The results describing the generation of the pre-SN model, the 1D SN model and the 2D interaction of the clump and shock, are presented in Section 3. Finally, in Sections 4 and 5, we discuss our findings and give a summary of the conclusions.

2 METHODS AND INITIAL CONDITIONS

We have modelled the interaction of an SN shell with a dense clump in three stages:

(i) the pre-SN phase, where the dynamical effects of photoionization heating from the star are modelled;

(ii) the post-SN phase, where the SN blast wave expands into the relic H II region left by the star; and

(iii) the shock-cloud interaction, where the expanding SN shell compresses a dense cloud.

The first two stages are simulated in one dimension with spherical symmetry, whereas the third stage is simulated in two dimensions with rotational symmetry. This is because compression and fragmentation of the clump cannot be captured within 1D models. However, it is possible to achieve a good representation of the evolution of the SN remnant in 1D models, assuming that the shell has not interacted with any dense clumps (Jun, Jones & Norman 1996).

For the 1D simulations, we use reflective boundary conditions at the origin (imposed by the symmetry of the problem), and a zero gradient outflow condition at the large radius boundary. For the 2D simulations with cylindrical coordinates (R, z), we use a reflective boundary at $R = 0$ (again imposed by symmetry) and zero gradient at $R = R_{\mathrm{max}}$, an inflow boundary at $z = z_{\mathrm{min}}$, and zero gradient at $z = z_{\mathrm{max}}$. The inflow boundary condition is justified because the post-shock flow variables change slowly for ≈ 5–7 pc behind the blast wave (see Fig. 2).

As argued in the Introduction, we do not expect HD cooling to be important because the SN shell and dense clump are exposed to UV radiation from the nearby relic H II region and expanding SN remnant. HD cooling is much more readily suppressed by UV radiation than H_2 cooling (Wolcott-Green et al. 2011), so we focus here only on the hydrogen and helium chemistry and cooling.

2.1 Pre-SN phase

We use the radiation-magnetohydrodynamics code PION (Mackey & Lim 2010, 2011) for the simulations presented here, first in 1D with spherical symmetry and later in 2D with rotational (axi-)symmetry. PION uses an explicit, finite-volume, integration scheme that is accurate to second order in time and space (Falle 1991). Here, only the Euler equations of hydrodynamics are solved, together with the ionization rate equation of hydrogen and associated non-equilibrium heating and cooling processes. The microphysical processes of ionization, recombination, heating and cooling are coupled to hydrodynamics using Algorithm 3 in Mackey (2012).

We consider a metal-free star exploding in a small galaxy at redshift $z = 10$, sweeping up the ambient medium to form an expanding shell. The simplified initial condition consists of a uniform neutral ISM with hydrogen number density $n = 10\,\mathrm{cm}^{-3}$. Into this, we place a dense cloud with (uniform) number density $n = 100\,\mathrm{cm}^{-3}$, radius $r_{\mathrm{c}} = 1.3$ pc, and located at $r = 40$ pc from the star (which is at the origin). The gas is comprised of atomic hydrogen and helium (number density ratio of 1.00:0.08) and is cooled via atomic processes. We assume that the star has formed in a sufficiently large galaxy that gravitational potential gradients can be neglected in the hydrodynamical evolution of the system. This is the simplest possible model for feedback from the massive star to a nearby cloud.

For the star's properties, we take the $40\,\mathrm{M}_\odot$ metal-free model from Schaerer (2002) with no mass-loss. This has a lifetime of 3.86 Myr, an effective temperature $T_{\mathrm{eff}} = 10^{4.9}\,\mathrm{K}$, and a time-averaged H-ionizing photon luminosity $Q_0 = 2.47 \times 10^{49}\,\mathrm{s}^{-1}$. For simplicity, we distribute these photons according to a blackbody spectrum with the star's T_{eff}. We ignore any post-main-sequence evolutionary effects because this comprises a small fraction of the star's life, and because the evolution is very uncertain. This model in Schaerer (2002) also remains relatively blue for its full lifetime, thus supporting our approximation of excluding a red supergiant phase.

2.2 SN remnant phase

An SN remnant is dominated by non-equilibrium cooling, therefore we developed a microphysics module which links the non-equilibrium chemistry and its associated cooling. This was accomplished by solving the following set of equations:

$$\frac{\partial E}{\partial t} = -\Lambda(\Sigma x_m, \rho, T) + \Gamma(\Sigma x_n, \rho, T) \tag{1}$$

$$\frac{\partial x_i}{\partial t} = C_i\left(x_j, \rho, T\right) - D_i\left(x_j, \rho, T\right) x_i, \tag{2}$$

where E is the internal energy density (in erg cm^{-3}), Λ is the cooling function of the gas (in erg cm^{-3} s^{-1}), Γ is the heating function of the gas (in erg cm^{-3} s^{-1}), x_i is the fractional abundance of a chemical species, i, for a total number of chemical species N_s, T is the temperature of the gas (K), ρ is the total mass density of the gas (g cm^{-3}), C is the formation rate of the species and D is the destruction rate of the species. We use a chemical network of 11 species (H, He, H_2, H^+, H_2^+, H_3^+, HeH^+, He^+, He^{++}, H^- and e^-) and 42 reactions. The chemical rates cover the temperature range 10–10^9 K, which are described in Appendix A. The atomic species and electron fraction are treated numerically as conservation equations.

The SN is modelled by injecting thermal energy, not kinetic (i.e. we ignore the free-expansion phase). Therefore, at very early times, the newly shocked gas has an artificially high temperature ($T > 10^9$ K), and at these temperatures, we utilize the value of the reaction rates at 10^9 K. To avoid artificial overcooling at early times, we only switch on the cooling when the gas adiabatically cooled down to 10^8 K. The thermal model includes atomic cooling (Fukugita & Kawasaki 1994; Hummer 1994), Bremsstrahlung cooling (Shapiro & Kang 1987; Hummer 1994), inverse Compton scattering (Peebles 1971) and molecular line cooling from H_2, H_2^+ and H_3^+ (Hollenbach & McKee 1979; Glover & Abel 2008; Glover & Savin 2009). The heating processes included in the model are cosmic microwave background (CMB) heating (assumed equal to $\Lambda(T_{\mathrm{CMB}})$) and cosmic ray heating (Glover & Jappsen 2007). We set the cosmic ray ionization rate at $\zeta = 10^{-18}\,\mathrm{s}^{-1}$ assuming the SN remnant to be their source. The chemical model, together with tests of the chemistry and dynamics, are presented in the appendices.

Both the 1D pre-SN and post-SN models consist of 5120 grid points to cover a 50 pc range, and are run until the SN shell reaches 4 pc from the clump centre. The output of this phase (ii) model (both chemical and dynamic properties) is then mapped on to a 2D grid which covers an area of 9.60×3.20 pc (480×160 grid zones, 0.02 pc per zone) to study the shock-cloud interaction (phase iii).

3 RESULTS

3.1 Pre-SN phase

The radial profile of the initial conditions and the pre-SN ISM are plotted in Fig. 1. The gas density inside the photoionized H II region ($r < 33$ pc) has decreased compared to the initial conditions (to close
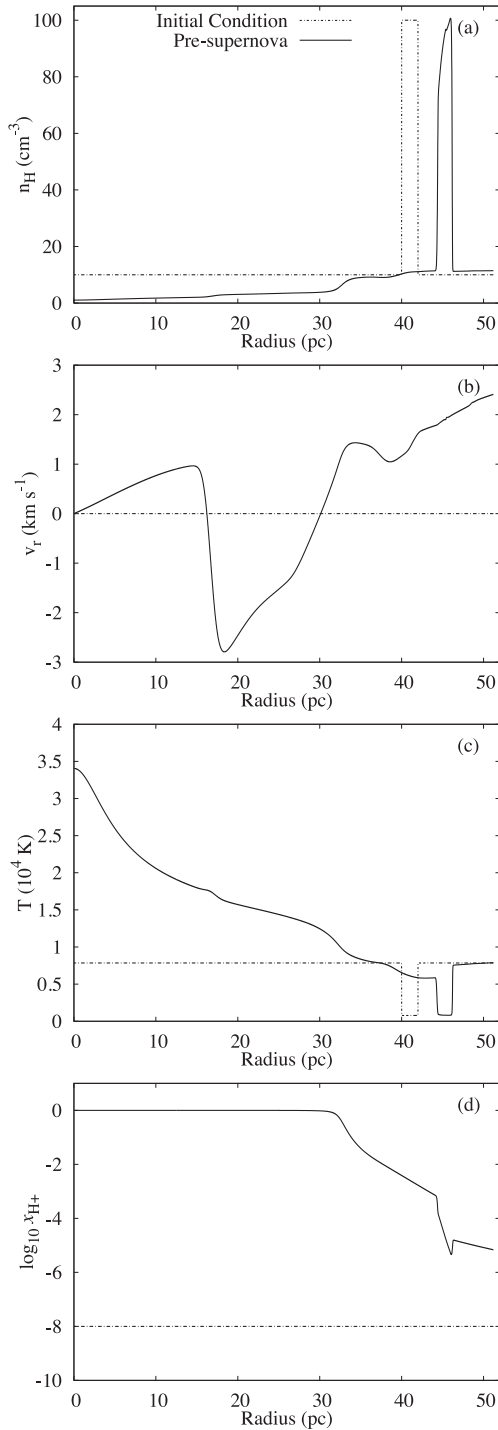
Figure 1. Plots of gas number density (a), velocity (b), temperature (c), and H$^+$ fraction (d) as a function of distance from the star. The dashed lines show the initial conditions and the solid lines the conditions at the pre-SN stage.

to $n = 1\,\mathrm{cm}^{-3}$) because photoheating has driven its expansion. In this phase, we only include atomic cooling, we assume that the H$_2$ within the gas has been destroyed as a result of Lyman–Werner radiation from the star. The shocked neutral ISM has only weak atomic coolants and so has not formed a shell, and remains very close to the initial ISM density. The cloud (or in 1D a shell) has been pushed outwards by the H II region expansion, and is moving
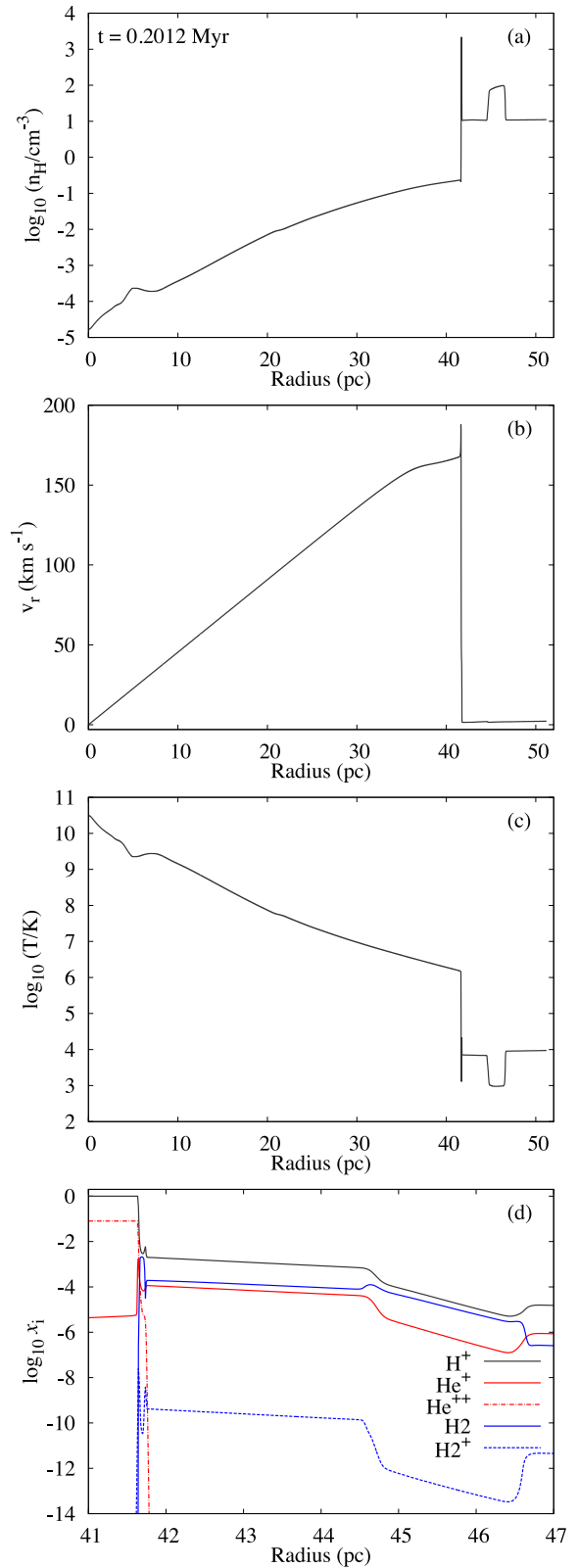
Figure 2. Gas number density (a), expansion velocity (b), temperature (c), and species fractions (d) as a function of distance from the star for the 1D post-SN evolution, at $t = 0.2012$ Myr after the SN explosion. Note that panel (d) has a different x-axis to the other panels, zoomed in to show only the chemistry of the SN shell and the overdense cloud (smaller and larger radii show little variation). The SN shell is at $r \approx 41.7$ pc, and the overdense cloud at $r \approx 44.6-46.6$ pc.

out at $v \approx 2$ km s^{-1} (Fig. 1b). The wave reflected back inwards is driving the negative velocity seen between $16 < r < 30$ pc, and this is a transient feature imposed by the assumed spherical symmetry (which forces waves to reflect back and forth between the origin and any strong discontinuities). It has little effect on the overall solution except to marginally increase the density in this radius range. The temperature profile of the H II region is typical of that produced by hot stars in metal-free gas (Iliev et al. 2006).

3.2 SN remnant phase

The output from the pre-SN model is utilized as the initial conditions of the 1D SN model. The clump has been moved to 45 pc due to the weak shock driven by dynamical expansion of the H II region (Fig. 1a). When mapping the chemical species, we assume the percentage of ionized hydrogen and helium (He$^+$) are equal, and the initial molecular fractions are set to zero. A 10^{52} erg explosion is initiated and a shell starts to form at around 27 pc. After 0.2012 Myr, the SN shock is well into the radiative phase, so a thin shell has formed that is about 200 times denser than the pre-shock gas. This agrees well with the isothermal shock jump conditions, where the overdensity is equal to the Mach number ($\mathcal{M}$) squared. In the shell, the isothermal sound speed is $a \approx 2.5$ km s^{-1}, so $\mathcal{M}^2 \approx (39/2.5)^2 \approx 240$. This is also similar to the maximum overdensity obtained from the test calculation in Appendix C. In the interior of the SN remnant, the usual Sedov–Taylor solution remains imprinted on the fluid quantities: the density and velocity tend to zero at the origin, and the temperature increases to maintain the constant interior pressure. The molecular fractions are all negligible in the hot interior, and have a maximum in the shocked shell because here the density is highest but there is also still a non-negligible electron fraction from heating in the shell's forward shock. The maximum H$_2$ fraction in the shell is $x(\mathrm{H_2}) \approx 0.002$, in agreement with previous work (Machida et al. 2005).

The 1D SN model is terminated when the shell reaches 41.9 pc (before it collides with the clump) and the output of this simulation (Fig. 2) is mapped on to a 2D axisymmetric grid. The initial conditions for the 2D model are outlined in Table 1. The SN shell is already travelling within the neutral ambient medium and is proceeding towards a dense spherical clump (~ 19 M$_\odot$) at a velocity of 39 km s^{-1}. The clump centre is 46 pc from the progenitor star. Fig. 3 displays the evolution of the clump as the SN shell collides and compresses it. The upper half-plane of the plots display the log of the number density ($\log_{10} n_{\mathrm{H}}$/cm^{-3}) and corresponding lower half-plane plots log of gas temperature reflected about the axis of symmetry. The black contour shows where the H$_2$ fraction equals 10^{-3}.

After 0.31 Myr, the shock has passed through half of the clump (upper plot in Fig. 3), we can see from Fig. 4 the maximum density of clump is ~ 6000 cm^{-3} with an associated temperature of ~ 1000 K.

Table 1. Initial conditions of 2D model.

Parameters	
Shell thickness	0.08 pc
Maximum shell density	1976 cm^{-3}
Minimum shell temperature	920 K
Shell velocity	39 km s^{-1}
Clump radius	1.3 pc
Maximum clump density	104 cm^{-3}
Minimum clump temperature	872 K
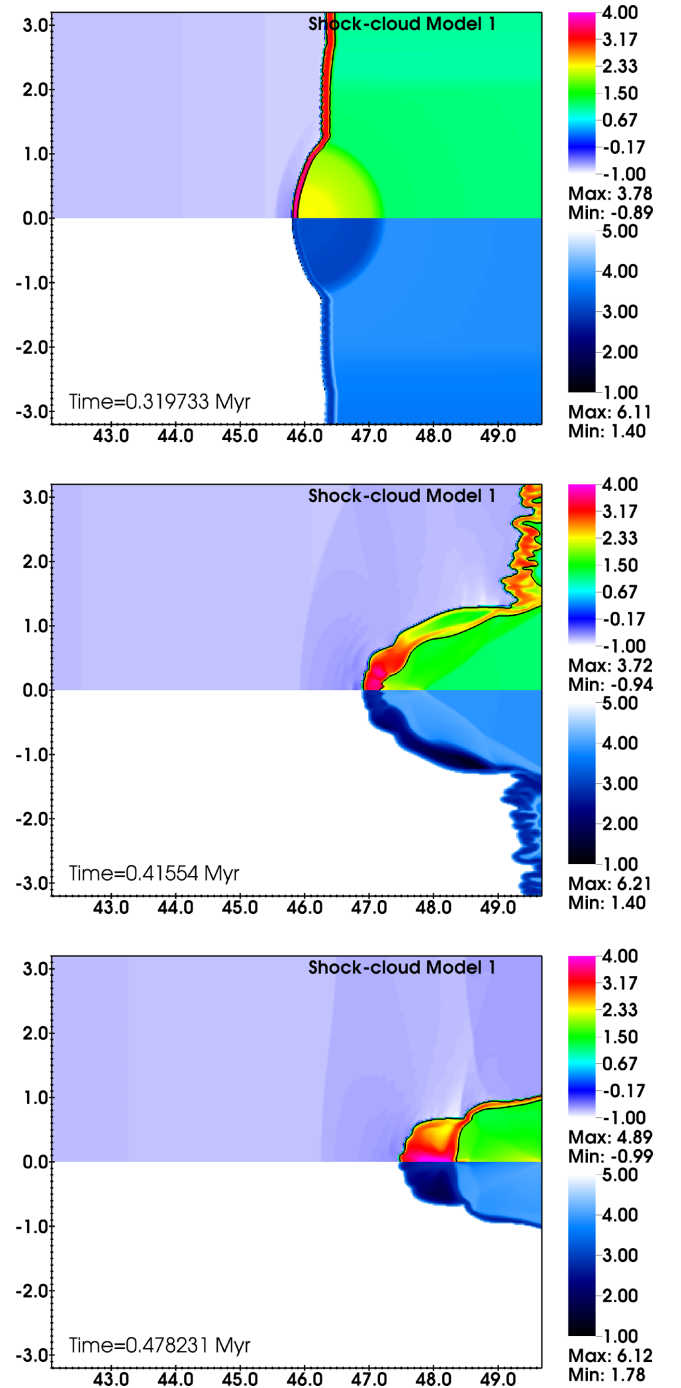
Figure 3. log of H number density ($\log_{10} (n_{\mathrm{H}}/\mathrm{cm}^{-3})$, colour scale) is plotted on the upper half-plane, and log of temperature on the lower half-plane (blue scale, in K), with a single black contour line overplotted on the upper half-plane showing where the H$_2$ fraction equals 0.001. The panels show an early time as the cloud is being shocked (top), after the shock has passed through the cloud (centre), and after the cloud has been compressed and accelerated by the shock (bottom). The x-axis shows distance from the star in parsecs, and the y-axis shows radial distance from the axis of symmetry of the 2D calculations (the lower half-plane is a reflection of the simulation domain to negative values).
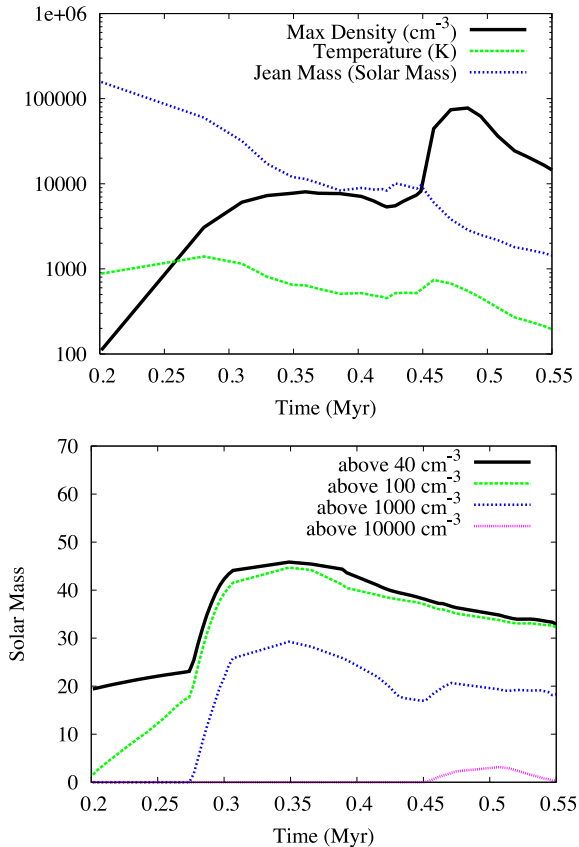
Figure 4. The upper plot displays the maximum density within the clump as the shock passes through, along with the temperature of the maximum density point and associated Jeans mass. The lower plot displays the mass within the clump as a function of different densities.

The SN shell has passed through the clump completely by 0.41 Myr (middle plot in Fig. 3), and due to the decline in pressure, the maximum density has decreased to ∼5200 cm^{-3}. The shock has caused an increase in free electrons, which catalyse the formation of H$_2$. Hence, the temperature of the high-density gas has decreased to ∼400 K. As the SN shell passes through and around the clump, the region of strong shear at the clump's edge undergoes adiabatic expansion and cools to close to the CMB temperature (middle panel of Fig. 3). This is not radiative cooling; the minimum temperature of the densest gas (with the strongest cooling) is ∼400 K. The clump reaches its maximum density of ≈78 000 cm^{-3} around 0.47 Myr after the initial SN explosion (bottom panel of Fig. 3). Again, we see that the densest gas is not the coldest gas, with a temperature of ∼300 K. The high-density gas (10^4 cm$^{-3} \lesssim n \lesssim 10^5$ cm^{-3}) does not cool below ∼148 K at any time. The re-expanding outer layers of the cloud are significantly colder with $T \approx 60$ K, because of adiabatic expansion. The turbulence that can be seen in the passing shock is due to the thin-shell instability. During the shock-cloud interaction, the clump mass has increased from 19 to 40 M$_\odot$. We do not expect this clump to be gravitationally unstable as the minimum Jeans mass is 1000 M$_\odot$ (Fig. 4).

After the passage of the shock, the dense cloud is embedded in the high-pressure, hot, low-density interior of the SN remnant. Our simulations do not have the spatial resolution to resolve the boundary layer between these two phases (we also do not include thermal conduction or model the external irradiation of the cloud), so the details of the boundary layer are probably not very reliable. The dominant physical process, however, is the simple pressure confinement of

the cloud, and this is well-captured by our calculation. By the time the cloud is accelerated off the simulation domain, it is entering an equilibrium phase of a pressure-confined cloud, similar to the cometary phase for irradiated clouds (Bertoldi & McKee 1990).

4 DISCUSSION

We have made a first investigation of the importance of non-equilibrium cooling processes occurring at all temperatures in primordial cloud-shock interactions (i.e. an SN shell interacting with primordial gas at redshift $z = 10$). This is an interesting case to study in its own right, for predicting the minimum mass that a metal-free star could potentially have. It is also the limiting case of considering shock-cloud interactions at extremely low metallicity, and so is useful for establishing a control simulation, against which models with non-zero metallicity can later be compared (Dhanoa & Mackey in preparation). The progenitor gas cloud for the hyper metal-poor star SDSS J102915+172927 (Caffau et al. 2011, with a total metallicity $Z \lesssim 10^{-5}$ Z$_\odot$) may have formed in a similar environment that was metal free, but which became slightly polluted with SN ejecta.

We include non-equilibrium chemistry to capture the radiative cooling occurring during the interaction of a shock and a small cloud, to establish if it is possible to form low-mass stars via this method. Considering a primordial chemistry for this process may be a simplification; because metals from the SN ejecta would interact and mix within the shell once the discontinuity between the shell and the ejecta is disrupted by the impact of the clump (Tenorio-Tagle 1996). However, the metallicity of the shell is expected to be near zero (Salvaterra, Ferrara & Schneider 2004) and according to Cen & Riquelme (2008), the shock velocity ensures that the clump remains mostly unaffected by metals. If this is true, then modelling the shock and cloud as metal free is a good approximation.

We calculate the minimum Jeans mass of the compressed clump with only H$_2$ cooling (i.e. the minimum possible), and therefore represent a limiting case for shock-cloud interactions for both low-metallicity models and primordial models which include deuterium cooling. We find that the fractional abundance of H$_2$ in the high-density region exceeds 3×10^{-3}, hence deuterium cooling may become important in this interaction (Nakamura & Umemura 2002). On the other hand, Wolcott-Green et al. (2011) have shown that HD cooling is suppressed by UV radiation fields that are five orders of magnitude weaker than what is required to suppress H$_2$ cooling. Thus, we expect that models with no HD cooling are applicable to a wider range of environments than models with HD cooling, once stars have begun forming in the vicinity.

We assume that the progenitor star is formed in a dark matter halo that is large enough so that edge effects do not need to be taken into account for a radius of $r \leq 50$ pc. Vasiliev et al. (2008) highlighted an important link between the radial distribution of primordial gas prior to the SN explosion and the subsequent evolution of the SN remnant; the state of the SN shell directly influences the formation of extremely metal-poor stars. This distribution is heavily dependent on the size of the H II region prior to the star's explosion. Studies which reproduce the abundance patterns in extremely metal-poor stars by modelling the evolution and explosion of metal-free stars (Nomoto et al. 2006; Joggerst, Woosley & Heger 2009; Joggerst et al. 2010), suggest that metal-poor stars are formed by metal-free stars within a mass range of 15–40 M$_\odot$. The explosion mechanism for metal-free stars is uncertain, especially above 30 M$_\odot$, and so the star can have a range of explosion energies from 0.6 to 10×10^{51} erg, which are associated with core collapse SNe and hypernovae.

Table 2. This table presents the initial conditions of a number of shock-cloud models and the corresponding fate of the clump at the end of the simulation. There are four end states of the clump: (i) the clump is unaffected by the shock as the shell stalled before reaching the clump, (ii) the clump is fully compressed into a single core, (iii) the clump fragments into smaller dense pieces and (iv) the clump no longer exists and is destroyed.

Model no.	SN energy (10^{51} erg)	Ambient cloud density (cm^{-3})	H II region included	Clump density (cm^{-3})	Temperature of clump (K)	Clump distance (pc)	Shock velocity (km s^{-1})	Clump fate
M01	10	10	Yes	100	872	46	39	compressed clump
M02	2.0	10	Yes	100	872	46	–	shell stalled
M03	1.0	10	Yes	100	872	46	–	shell stalled
M04	0.6	10	Yes	100	872	46	–	shell stalled
M05	10	1	No	100	200	50	200	destroyed
M06	2.0	1	No	100	200	50	46	small fragments
M07	1.0	1	No	100	200	50	26	destroyed
M08	0.6	1	No	100	200	50	16	destroyed
M09	1.0	1	No	100	200	40	49	small fragments

A clump initially at distance $r \geq 40$ pc from the star can safely be assumed to be neutral, because Fig. 1 shows that the clump does not interact with any ionizing radiation. Clouds found closer to the progenitor star may evaporate, or at a minimum, have a different thermal state to a neutral cloud. Radiation between 11.18 and 13.6 eV photodissociates H_2 molecules and so has a knock-on heating effect on the gas. This dissociation radiation propagates further than ionizing radiation, and without any dust present, we expect that clump is completely atomic in the pre-SN stage. In the 2D model, dissociative photons from the hot gas are assumed to be negligible (Vasiliev et al. 2008), but the possible effects of UV radiation on the clump should be investigated in more detail in future work.

After exploring a number of explosion energies (see models M01−M04 in Table 2), we found that only the shock formed from a hypernova explosion (10^{52} erg) reached and compressed the clump. When extending our study by exploring other ambient cloud densities (models M05−M09 in Table 2), it emerges that the shock velocity determines the fate of the neutral clump. If the shock is too fast, the clump is destroyed. When the SN shock is too slow, the clump is only slightly compressed but inevitably destroyed. This is because the initial shock causes a secondary shock to travel through the rest of the clump, finally the gas disperses and flows downstream with the SN shock. We therefore find that a small range of shock velocities (30−50 km s^{-1}) which can cause the clump to compress or fragment. Here, the cooling time is equal to or less than the collapse/compression time and the velocity of the shock causes at least half of the clump to be compressed. Shock velocities above 40 km s^{-1} cause the clump to fragment into smaller clumps, while below this velocity, we find that the clump is compressed.

The clump is near an SN remnant so it will be exposed to cosmic rays, but the cosmic ray spectrum and intensity is unknown because of uncertainties in the expected interstellar magnetic field and the explosion mechanism for metal-free stars. We have assumed the spectrum to be close to the observed spectrum in the Galactic environment, in keeping with Stacy & Bromm (2007). In this model, we include a background cosmic ray ionization rate of 10^{-18} s^{-1}, as this rate was found to produce an overall cooling effect. We have not explored X-rays in this work, which would be produced by the SN remnant. This would increase the H_2 abundance of gas ahead of the shell by increasing the free electron content (Haiman, Rees & Loeb 1997; Ferrara 1998) and should be subject to further investigation. The effects of a range of cosmic ray ionization rates (10^{-18}–10^{-15} s^{-1}) and their associated heating on the shock-clump interactions will also be explored in future work.

The shocked clump of model M01 implodes because of the passage of the SN shock (Fig. 3). This is the same behaviour as

seen in 3D simulations of clouds interacting with clumps (Melioli et al. 2006; Leão et al. 2009; Johansson & Ziegler 2013), and earlier 2D work (e.g. Klein et al. 1994). We find that in our simulation that the clump gains a maximum density of $\sim$78 000 cm^{-3}, which is a density enhancement of $10^{2.89}$ but does not become Jeans unstable. Vaidya et al. (2013) show that self-gravity has no effect on the clump at this point of the shock interaction, where the implosion is pressure driven and the clump reaches its maximum density. This gives us confidence that the implosion phase is correctly captured by our simulation. Johansson & Ziegler (2013) investigate the compression of an $n = 17$ cm^{-3} cloud (with radius 1.5 pc) and find higher density enhancements of 10^3–10^5. They also conclude that the clump will not become Jeans unstable. It is worth noting that their work considers solar metallicity gas with an equilibrium cooling function. Hence, this may change when the model is refined to include non-equilibrium cooling.

Dust is assumed to be the major coolant in low-metallicity environments (Klessen et al. 2012; Schneider et al. 2012). How quickly it can form in a primordial SN ejecta and the extent of mixing that would occur during this cloud-shock interaction are still open questions. It is believed that dust is quickly destroyed in the reverse shocks formed when the SN shell begins to travel within the multiphase neutral medium (Cherchneff & Dwek 2010; Silvia, Smith & Shull 2010). Without much dust in the environment, we cannot expect metal-line cooling to drastically lower the Jean mass, especially at metallicities $\leq 10^{-5}$ Z$_\odot$. In light of this, much further work is required to investigate the effects of cosmic rays and external radiation fields (especially X-ray and UV) on this process, because there may be important positive feedback effects (Ricotti, Gnedin & Shull 2002; O'Shea et al. 2005) that have not been considered so far.

5 CONCLUSION

We have presented a metal-free shock-cloud model, which simulates an SN remnant interacting with a cloud at redshift $z = 10$. We model a dense clump ($n = 100$ cm^{-3}, $r = 1.3$ pc) embedded in a 10 cm^{-3} ambient cloud, which is 40 pc from the progenitor star. We consider realistic pre-SN conditions by including the effects of stellar radiation from a 40 M$_\odot$ metal-free star on the multiphase neutral medium. At the end of the star's main-sequence lifetime, a hypernova (10^{52} erg) is initiated and the evolution of the SN shell and its subsequent interaction with the dense clump is studied. Radiative cooling is a crucial process in the shock-cloud interaction, allowing the formation of dense cold gas that may be susceptible to gravitational collapse. During this process, we have

comprehensively modelled the radiative (non-equilibirum) cooling taking place.

We followed the evolution of the SN remnant and its interaction with the surrounding ionized and neutral medium. When the radiative shell interacts with the metal-free clump, it reaches a maximum of density $\sim 78\,000\ \mathrm{cm^{-3}}$. This is a $10^{2.89}$ density enhancement and is consistent with Galactic shock-cloud models considering solar metallicity gas with equilibrium cooling functions. The clump undergoes a reduction in Jeans mass from 10^5 to $10^3\ \mathrm{M_\odot}$, but does not become gravitationally unstable. Further work is required to ascertain the effect of cosmic rays, X-rays and UV radiation on the clump during the SN phase.

In this work, we found an optimal range of shock velocities (30–50 km s^{-1}) which compress small metal-free clouds. Below this range, the cloud is slightly perturbed by the SN shock and is not subject to any appreciable density enhancement. Above this range, the clumps are destroyed, therefore the results by Mackey et al. (2003) are overoptimistic, as they assume that the cloud survives a 200 km s^{-1} interaction.

In this initial study, we have only considered a single clump with fixed radius and density, varying the SN energy and the density of the medium that the clump is embedded in. We have shown that the Jeans mass is indeed reduced significantly by the shock-cloud interaction, but not sufficiently to form stars with $<1\ \mathrm{M_\odot}$. In order to draw more general conclusions about the possibility of forming such low-mass stars from metal-free gas, we plan to follow up this work by considering a range of clump sizes and central densities.

When investigating model M01, we have achieved an appreciable Jean mass reduction of a small dense clump and a density enhancement comparable to Galactic studies, by including non-equilibrium metal-free radiative cooling. Further refinement of this model by including low-metallicity chemistry plus positive feedback effects from cosmic rays, X-rays and UV radiation, may cause a further reduction in Jeans mass. Galactic models should be extended to include non-equilibrium cooling, as this work has shown that it is the dominant process in shock-cloud interactions.

REFERENCES

Bertoldi F., McKee C. F., 1990, ApJ, 354, 529
Caffau E. et al., 2011, Nature, 477, 67
Cen R., Riquelme M. A., 2008, ApJ, 674, 644
Cherchneff I., Dwek E., 2010, ApJ, 713, 1
Chiaki G., Yoshida N., Kitayama T., 2013, ApJ, 762, 50
Falle S. A. E. G., 1991, MNRAS, 250, 581
Ferrara A., 1998, ApJ, 499, L17
Fukugita M., Kawasaki M., 1994, MNRAS, 269, 563
Galli D., Palla F., 1998, A&A, 335, 403
Glover S. C. O., Abel T., 2008, MNRAS, 388, 1627
Glover S. C. O., Jappsen A.-K., 2007, ApJ, 666, 1
Glover S. C. O., Savin D. W., 2009, MNRAS, 393, 911
Greif T. H., Johnson J. L., Klessen R. S., Bromm V., 2008, MNRAS, 387, 1021
Haiman Z., Rees M. J., Loeb A., 1997, ApJ, 476, 458
Hollenbach D., McKee C. F., 1979, ApJS, 41, 555
Hummer D. G., 1994, MNRAS, 268, 109
Iliev I. T. et al., 2006, MNRAS, 371, 1057
Joggerst C. C., Woosley S. E., Heger A., 2009, ApJ, 693, 1780
Joggerst C. C., Almgren A., Bell J., Heger A., Whalen D., Woosley S. E., 2010, ApJ, 709, 11
Johansson E. P. G., Ziegler U., 2013, ApJ, 766, 45
Jun B.-I., Jones T. W., Norman M. L., 1996, ApJ, 468, L59
Kitayama T., Yoshida N., 2005, ApJ, 630, 675
Klein R. I., McKee C. F., Colella P., 1994, ApJ, 420, 213
Klessen R. S., Glover S. C. O., Clark P. C., 2012, MNRAS, 421, 3217
Leão M. R. M., de GouveiaDal Pino E. M., Falceta-Gonçalves D., Melioli C., Geraissate F. G., 2009, MNRAS, 394, 157
Machida M. N., Tomisaka K., Nakamura F., Fujimoto M. Y., 2005, ApJ, 622, 39
Mackey J., 2012, A&A, 539, A147
Mackey J., Lim A. J., 2010, MNRAS, 403, 714
Mackey J., Lim A. J., 2011, MNRAS, 412, 2079
Mackey J., Bromm V., Hernquist L., 2003, ApJ, 586, 1
Melioli C., de GouveiaDal Pino E. M., de La Reza R., Raga A., 2006, MNRAS, 373, 811
Nagakura T., Hosokawa T., Omukai K., 2009, MNRAS, 399, 2183
Nakamura F., Umemura M., 2002, ApJ, 569, 549
Nomoto K., Tominaga N., Umeda H., Kobayashi C., Maeda K., 2006, Nucl. Phys., 777, 424
O'Shea B. W., Abel T., Whalen D., Norman M. L., 2005, ApJ, 628, L5
Peebles P. J. E., 1971, Physical Cosmology. Princeton Univ. Press, Princeton, NJ
Raga A. C., Cantó J., Rodríguez L. F., Velázquez P. F., 2012, MNRAS, 424, 2522
Reach W. T., Rho J., Jarrett T. H., 2005, ApJ, 618, 297
Ricotti M., Gnedin N. Y., Shull J. M., 2002, ApJ, 575, 49
Salvaterra R., Ferrara A., Schneider R., 2004, New Astron., 10, 113
Sánchez-Salcedo F. J., Vázquez-Semadeni E., Gazol A., 2002, ApJ, 577, 768
Schaerer D., 2002, A&A, 382, 28
Schneider R., Omukai K., Limongi M., Ferrara A., Salvaterra R., Chieffi A., Bianchi S., 2012, MNRAS, 423, L60
Shapiro P. R., Kang H., 1987, ApJ, 318, 32
Silvia D. W., Smith B. D., Shull J. M., 2010, ApJ, 715, 1575
Slyz A. D., Devriendt J. E. G., Bryan G., Silk J., 2005, MNRAS, 356, 737
Stacy A., Bromm V., 2007, MNRAS, 382, 229
Stacy A., Bromm V., 2014, ApJ, 785, 73
Sutherland R. S., Dopita M. A., 1993, ApJS, 88, 253
Tenorio-Tagle G., 1996, AJ, 111, 1641
Vaidya B., Hartquist T. W., Falle S. A. E. G., 2013, MNRAS, 433, 1258
Vasiliev E. O., Vorobyov E. I., Shchekinov Y. A., 2008, A&A, 489, 505
Verner D. A., Ferland G. J., 1996, ApJS, 103, 467
Voronov G. S., 1997, At. Data Nucl. Data Tables, 65, 1
Wolcott-Green J., Haiman Z., Bryan G. L., 2011, MNRAS, 418, 838
Woodall J., Agúndez M., Markwick-Kemper A. J., Millar T. J., 2007, A&A, 466, 1197

APPENDIX A: CHEMISTRY NETWORK

The full chemical network is displayed in Table A1. All the molecular reaction rates (R07–R42) have been adapted for the temperature range (10–10^9 K) and have been divided into two categories: (i) formation rates (listed in Table A2) and (ii) destruction rates (listed in Table A3).

Table A1. Metal-free chemistry network.

Reaction no.	Reaction	References for rate coefficients
R01	$H^+ + e^- \rightarrow H + \gamma$	H
R02	$He^+ + e^- \rightarrow He + \gamma$	VF
R03	$He^{++} + e^- \rightarrow He^+ + \gamma$	VF
R04	$H + e^- \rightarrow H^+ + e^- + e^-$	V
R05	$He + e^- \rightarrow He^+ + e^- + e^-$	V
R06	$He^+ + e^- \rightarrow He^{++} + e^- + e^-$	V
R07	$H_2 + H \rightarrow H + H + H$	GA08
R08	$H^- + H \rightarrow H + H + e^-$	GA08
R09	$H^- + He \rightarrow He + H + e^-$	GA08
R10	$H_2 + H_2 \rightarrow H_2 + H + H$	UM06
R11	$H^- + e^- \rightarrow H + e^- + e^-$	JR
R12	$H_2 + He^+ \rightarrow He + H^+ + H$	UMO6
R13	$H_2 + e^- \rightarrow H + e^- + H$	UM06
R14	$H_2^+ + e^- \rightarrow H^+ + e^- + H$	R14*
R15	$HeH^+ + e^- \rightarrow He^+ + e^- + H$	R14*
R16	$H^+ + H \rightarrow H_2^+ + \gamma$	UM06, GA08
R17	$H^+ + He \rightarrow HeH^+ + \gamma$	UM06
R18	$H + e^- \rightarrow H^- + \gamma$	UM06, GA08
R19	$HeH^+ + e^- \rightarrow He + H$	UM06
R20	$H_2^+ + e^- \rightarrow H + H$	UM06
R21	$H_3^+ + e^- \rightarrow H + H + H$	UM06
R22	$H_3^+ + e^- \rightarrow H_2 + H$	UM06
R23	$H^- + H_2^+ \rightarrow H + H + H$	GA08
R24	$H + He^+ \rightarrow He + H^+$	UM06,hd
R25	$H_2 + He^+ \rightarrow He + H_2^+$	UM06
R26	$H^+ + H^- \rightarrow H + H$	UM06
R27	$H^- + H_2^+ \rightarrow H_2 + H$	UM06
R28	$H^- + He^+ \rightarrow He + H$	UM06
R29	$H + H_2^+ \rightarrow H_2 + H^+$	UM06
R30	$H_2^+ + H_2 \rightarrow H_3^+ + H$	UM06
R31	$H^- + H_3^+ \rightarrow H_2 + H_2$	UM06
R32	$H + HeH^+ \rightarrow He + H_2^+$	UM06
R33	$H_2 + HeH^+ \rightarrow He + H_3^+$	UM06
R34	$H_2^+ + He \rightarrow HeH^+ + H$	UM06
R35	$H^- + H^+ \rightarrow H_2^+ + e^-$	SK87
R36	$H^- + H \rightarrow H_2 + e^-$	UM06
R37	$H + CR \rightarrow H^+ + e^-$	UM06
R38	$He + CR \rightarrow He^+ + e^-$	UM06
R39	$H_2 + CR \rightarrow H^+ + H + e^-$	UM06
R40	$H_2 + CR \rightarrow H + H$	UM06
R41	$H_2 + CR \rightarrow H^+ + H^-$	UM06
R42	$H_2 + CR \rightarrow H_2^+ + e^-$	UM06

References – UM06 = UMIST data base for astrochemistry [rate 06, non-dipole enhanced] (Woodall et al. 2007); GA08 = Glover & Abel (2008); H = Hummer (1994); GP98 = Galli & Palla (1998); SK87 = Shapiro & Kang (1987); hd = matching scheme; R14* = same value as R14; JR = private communication with Jonathan Rawlings; V = Voronov (1997); VF = Verner & Ferland (1996).

Most of the UM06 rates are valid until 41 000 K. If a formation rate is valid up to a lower temperature, the value at the maximum temperature range is kept constant for temperatures until 41 000 K. Above 41 000 K, all formation rates are cut-off and the reaction rates take on the following forms:

$$K_1 = k \times \exp\left(1.0 - \frac{T}{41\,000.0}\right)$$

$$K_2 = k \times \exp\left(10 \times \left(1.0 - \frac{T}{41\,000.0}\right)\right),$$

where k is the value of the rate at 41 000 K. The details of how each formation reaction is treated, can be found in Table A2.

The destruction rates are extrapolated above their valid temperature range. Above this temperature, if there is a maximum value after which the rate decreases (T_{ex}), this maximum value is kept constant for all higher temperatures ($T > T_{ex}$). All the destruction rates, with the corresponding maximum extrapolation temperatures and temperatures ranges are displayed in Table A3.

APPENDIX B: COOLING TEST

Fig. B1 displays a comparison of the primordial chemistry network presented in this work (DMY) and that of Glover & Abel (2008, GA) which includes 32 reactions that contain hydrogen and helium species only. The GA deuterium reactions are not included. Notably, GA have included three-body reactions and density-dependent

Table A2. Molecular reactions that are cut-off at 41 000 K: E = rate extrapolated; C = max/min value kept constant and extended; − = Not applicable; S = switching between different reaction rates within temperature range; CT2 = $k\exp(10.0 \times (1.0 - T/41\,000))$ and CT = $k\exp(1.0 - T/41\,000)$ are exponential cut-off for $T > 41\,000$ K and k is the value of the reaction rate at 41 000 K

Reaction number	Valid temperature range (K)	Below minimum temperature	Above maximum temperature	Cut-off type $T > 41\,000$ K
R16	S:10–32 000	–	C	CT2
R17	16–100	C	E	CT
R18	S:10–41 000	–	–	CT2
R29	10–41 000	–	–	CT
R30	10–41 000	–	–	CT
R33	10–41 000	–	–	CT
R34	10–41 000	–	–	CT
R35	10–41 000	–	–	CT
R36	S:10–41 000	–	–	CT

Table A3. Molecular reactions adapted to maximum temperature (10^9 K): E = rate is extrapolated to a maximum Extrapolation Temperature (T_{ex}) and then extended as a constant after that temperature; C = max/min value kept constant; − = Not applicable; S = a number of reaction rates utilized within temperature range.

Reaction number	Valid temperature range of rate (K)	Below range	Above range	Maximum extrapolation temperature T_{ex} (K)
R07	1833–41000	E	E	10^9
R08	10–10000	–	C	–
R09	10–10000	–	C	–
R10	2803–41000	E	E	10^7
R11	10–41000	–	E	10^5
R12	100–300	E	E	10^8
R13	3400–41000	E	E	10^8
R14	3400–41000	E	E	10^8
R15	3400–41000	E	E	10^8
R19	10–300	-	E	10^9
R20	10–300	–	E	10^9
R21	10–1000	–	E	10^9
R22	10–1000	–	E	10^9
R23	10–10000	–	C	–
R24	S:10–41000	–	C	–
R25	10–300	–	E	10^9
R26	10–300	–	E	10^4
R27	10–300	–	E	10^9
R28	10–300	–	E	10^9
R31	10–300	–	E	10^9
R32	10–41000	–	E	10^9
R37	10–41000	–	C	–
R38	10–41000	–	C	–
R39	10–41000	–	C	–
R40	10–41000	–	C	–
R41	10–41000	–	C	–
R42	10–41000	–	C	–

reactions for

$$H_2 + H_2 \rightarrow H + H + H_2$$
$$H_2 + He \rightarrow H + H + He.$$
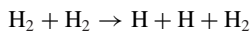
These reactions have been neglected in our network. However, Glover & Abel (2008) do not include H_3^+ and HeH^+.

In this test, we adopt a one-zone constant density model, where both chemistry networks are linked to the same set of cooling functions, i.e. the H_2 and H_2^+ cooling functions provided by Glover

& Abel (2008) and Hollenbach & McKee (1979) plus the atomic cooling functions given by Fukugita & Kawasaki (1994), Hummer (1994), Shapiro & Kang (1987) and Peebles (1971). The initial temperature of the gas is 10^4 K and three densities are investigated: $n = 1, 100, 10^4$ cm^{-3}. The gas is allowed to chemically evolve and cool over 5×10^7 yr.

For the low-density test (i.e. $n = 1$ cm^{-3}), both microphysics modules reach the same temperature of 244 K. In the test for $n = 10^4$ cm^{-3}, the temperatures are very close; our module cools
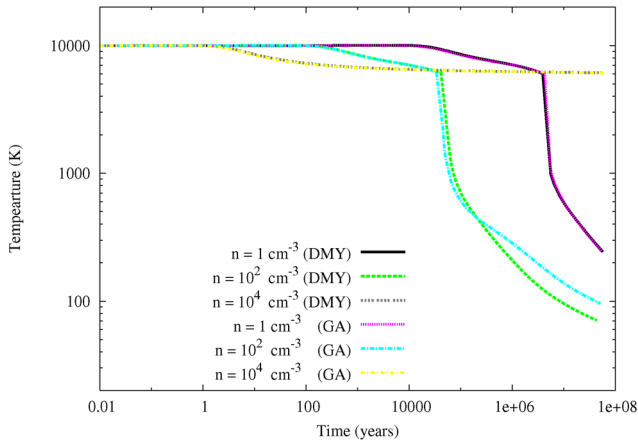
Figure B1. One-zone test to compare the microphysics module (DMY) against the chemistry network presented by Glover & Abel (2008, GA). Both networks use the same cooling rates for each species. The gas is initially fully ionized and has a temperature of 10^4 K. Three different densities are investigated: $n = 1$, 100 and 10^4 cm^{-3}.

down to 6115 K and the GA module cools to 6090 K. At this density, the H_2 cooling is within the local thermodynamic equilibrium regime. The temperatures are very close, the difference is due to the rates we have included and not because the three-body reactions were excluded. Three-body reactions are dominant for densities $n \geq 10^5$ cm^{-3}, and can be neglected as we do not expect the densities in the module to reach this value. Finally, for $n = 100$ cm^{-3}, we obtain 69 K whilst the GA module obtains 90 K. When we include the reactions that are missing from our module, we still obtain 69 K. This highlights that the differences in temperature are due to the differences between the rates used in UM06 data base and the GA module.

APPENDIX C: 1D SN SHELL EXPANSION

Fig. C1 shows the results of a 1D test, in which the expansion of a blastwave is followed using different chemistry/cooling assumptions: adiabatic with no chemistry, including chemistry but only atomic coolants, and including chemistry with atomic and molecular coolants. The radius of the SN forward shock (upper panel) and maximum density in the shell (lower panel) are plotted as a function of time since explosion. We used uniform radial grid with 5120 grid zones between $r = 0$ and 130 pc, and input 10^{51} ergs of thermal energy in the eight grid zones closest to the origin. The ISM is a constant density medium with $\rho = 2.44 \times 10^{-24}$ g cm^{-3} at a redshift of 20. The initial ISM temperature is $T = 10^4$ K (corresponding to a pressure of $p \approx 1.5 \times 10^{-12}$ dyne cm^{-2}). Without any cooling, this can be compared to the Sedov–Taylor solution, and when cooling and chemistry are included, we compare to the results of Machida et al. (2005).

The adiabatic calculation matches the Sedov–Taylor solution until about 0.8 Myr, after which the shock runs ahead of this solution. The explanation for this is that the shock weakens as it slows down at late times, and the ISM ambient pressure is no longer negligible. This breaks the scale-free nature of the analytic solution, and the result is that the shock radius advances faster than predicted at late times (cf. Raga et al. 2012).

At about 0.05 Myr, the simulations with cooling start to decelerate and deviate from the adiabatic solution. The expansion rate
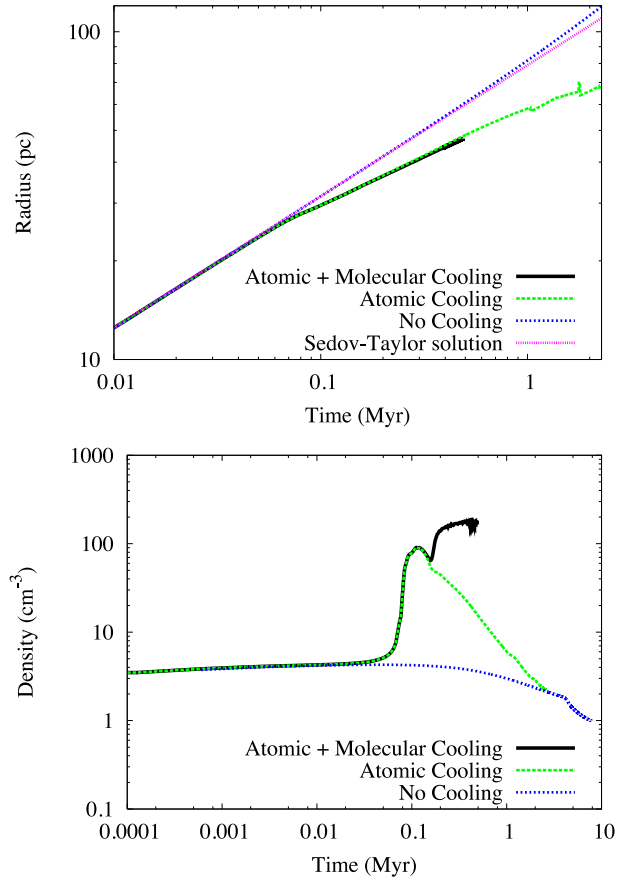
Figure C1. SN shell expansion as a function of time for an adiabatic calculation, a calculation with atomic line cooling only, and a calculation with atomic and molecular cooling switched on. The expansion radius is compared to the analytic Sedov–Taylor solution in the upper plot. The lower plot shows the maximum gas number density in the shell as a function of time for the same three models.

changes from the Sedov–Taylor value $R_{sh} \propto t^{2/5}$ to the momentum-conserving value $R_{sh} \propto t^{1/4}$. Atomic cooling is initially much stronger than molecular cooling, so both of these runs match each other until the molecular cooling begins to affect the shell and the ISM at $t \approx 0.2$ Myr. At later times, the shell density in the cooling model decreases steadily because it can no longer cool, and the weak forward shock keeps adding lower entropy gas to the shell. The molecular cooling model has a higher density shell once molecular cooling becomes important at $t \approx 0.2$ Myr, because it can cool to much lower temperatures. This has the further effect that the shell remains at a high density for much longer.

The molecular cooling calculation shows that we get compression factors of >100 times in the shell at $t \geq 0.2$ Myr. This model disagrees strongly with Machida et al. (2005, see their fig. 4), who found only weak density increase in the SN shell for times up to 10^7 yr. The density in their analytic model was set by the imposed pressure-confining boundary conditions on the shell, so we suspect that one of the boundary conditions was incorrect.

This paper has been typeset from a TEX/LATEX file prepared by the author.